J. Fluid Mech. (2007), *vol.* 587, *pp.* 1–22.
doi:10.1017/S002211200700657X Printed in the United Kingdom

Dynamics of droplet–film collision

K. L. PAN† AND C. K. LAW

Department of Mechanical and Aerospace Engineering, Princeton University, Princeton, NJ 08544, USA

(Received 8 September 2006 and in revised form 14 March 2007)

The head-on collision of a droplet onto a liquid layer of the same material, backed by a solid surface, was experimentally and computationally investigated, with emphasis on the transition from bouncing of the droplet to its absorption by the film for given droplet Weber number, We, and the film thickness scaled by the droplet radius, H_f. Experimental results show that while absorption is favoured with increasing We, there exists a range around $H_f \approx 1$ over which this tendency is moderated. This local moderation in turn corresponds to a regime, $11 \lesssim We \lesssim 14$, over which increasing H_f from a small value leads to a triple reversal behaviour of absorption, bouncing, absorption again, and bouncing again. The collision dynamics including evolution of the surface contours of the droplet and film, as well as the energy budgets, were then simulated by using a front-tracking technique. For collisions leading to absorption and partial absorption, for which part of the absorbed droplet is subsequently ejected from the film, rupture and hence merging of the interfaces were manually imposed at an instant that leads to agreement between the subsequent calculated and experimental images. The simulation satisfactorily identified the different factors influencing the observed non-monotonic response of the collision event.

1. Introduction

The collision dynamics of droplets on liquid and solid surfaces is of relevance to a variety of natural phenomena and technological applications such as spray combustion in liquid-fueled combustors, ink-jet printing, raindrop interaction with ocean and soil surfaces, insecticide spraying, meteorite impaction, spray painting and coating, etc. Earlier studies were primarily concerned with water in air (Jayaratne & Mason 1964; Stow & Hadfield 1981) because of the prevalence of water and its relevance to meteorological implications. Results showed that, depending on such parameters as the impact inertia, surface tension, and impact angle, collision can result in bouncing, absorption by the liquid layer, and splashing (Rein 1993; Stanton & Rutland 1998). The controlling dynamic parameter is the collision Weber number, defined as $We = 2\rho_\ell V_0^2 R/\sigma$, where R is the droplet radius, V_0 the impact velocity, and ρ_ℓ and σ the density and surface tension of the liquid, respectively. Studies involving head-on collisions (Harlow & Shannon 1967; Rodriguez & Mesler 1985) were mostly concerned with the transition between absorption and splashing that occurs at high We. Bouncing was observed at lower values of We (Ching, Golay & Johnson 1984), although its characteristics, including the transition to merging, have not been sufficiently studied.

† Present address: Department of Mechanical Engineering, National Taiwan University, Taiwan.

It is reasonable to expect that some aspects of the droplet–film collision should be analogous to those of droplet–droplet collision, which has been extensively studied, with some recent work reported in, for example, Ashgriz & Poo (1990), Jiang, Umemura & Law (1992), Qian & Law (1997), Orme (1997), Pan (2004), and Pan & Law (2004). Specifically, for head-on collisions, four distinct regimes were observed with increasing *We*, namely: (I) permanent merging after minor droplet deformation, (II) bouncing, (III) permanent merging after substantial droplet deformation, (IV) merging followed by separation and the concomitant production of secondary droplets. Furthermore, it was demonstrated that the propensity for bouncing or merging is a result of the readiness with which the gaseous mass in the inter-droplet gap can be squeezed out of the gap by the colliding interfaces such that they can make contact and hence merge.

In view of the considerable understanding that has been gained on droplet–droplet collision, we now progress to the study of droplet–film collision. We are particularly interested in a liquid surface of finite thickness, backed by a solid surface, so as to simulate the practical situation of droplets impacting a solid surface that has been wetted by the arrival of previous droplets. We shall show that while the experimental collision outcome approaches the deep-pool situation in which bouncing and absorption are respectively favoured for small and large Weber numbers, there exists an intermediate range in *We* for which the response can be highly non-monotonic when the film thickness, h_f, is either of the same magnitude as, or smaller than, the droplet radius. In particular, as h_f progressively increases from a small value, for a fixed *We*, the collision results in absorption, bouncing, and absorption again before reaching the deep-pool, bouncing limit. Partial absorption, in which a secondary droplet is ejected after the initial absorption of the impacting droplet, was also observed. We shall then use a front-tracking technique to computationally investigate the collision dynamics in terms of the interfacial contour and the energy budget.

2. Experimental specifications

Similar to the study of droplet–droplet collision (Jiang *et al.* 1992), in the present investigation droplets were generated through a nozzle triggered by the vibration of a piezoelectric diaphragm. Nozzles of different diameters, ranging from 180 to 310 μm, were used, generating droplets of uniform diameters that ranged from 250 to 650 μm. Droplets of tetradecane or dodecane, which are representative of the volatilities of diesel fuels, were ejected downward from the nozzle at a certain height onto a brass plate covered by a thin layer of the same liquid. The film thickness was determined by calculating the known amount of liquid spread on the plate surface based on the area of the film, assuming uniform distribution. The calculated thickness was further verified by measuring it microscopically. Only head-on collision events were studied, and only results on tetradecane are reported because those on dodecane are qualitatively similar.

Imaging of the collision sequence was not acquired through stroboscopy synchronized with the droplet generation circuit, which was the technique used in the droplet–droplet experiments (Jiang *et al.* 1992). This is because the shape and thickness of the film can be substantially distorted by the continuous deposition of the droplets. Furthermore, when the head-on collision results in re-bouncing of the droplet from the surface, the upwardly moving, re-bouncing droplet will collide with the downwardly moving, incoming droplet because they travel along the same

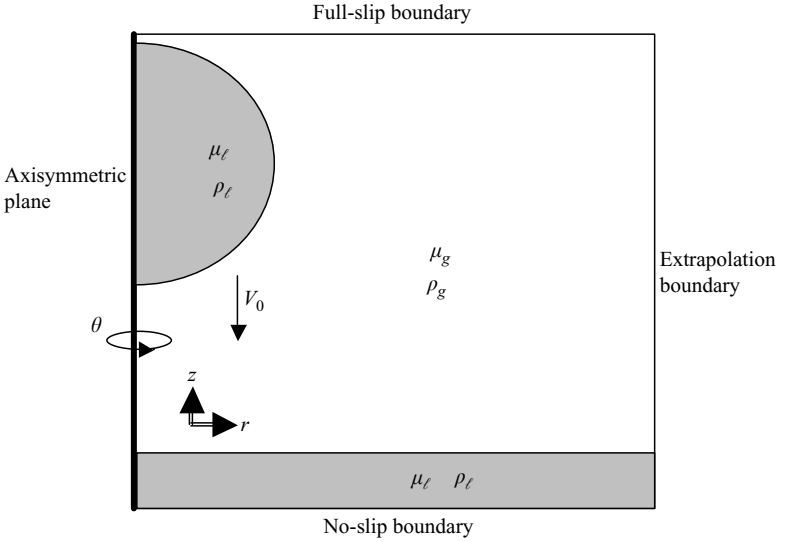

FIGURE 1. Schematic of the computational domain for droplet–film collision.

collinear path. Consequently it is necessary to record the collision sequence of a single droplet. We have therefore adapted a high-speed digital camera mounted on a microscopic imaging system to capture the transient images of the colliding event of an individual droplet. The camera has a maximum framing rate of 8000 frames per second (f.p.s.) and a minimum exposure time of 1/80 000 s. The experimental sequences reported herein were usually recorded with 4000 f.p.s. and 50 μs exposure time.

3. Formulation and numerical specifications

The collision event was simulated by the front-tracking method previously applied to droplet–droplet collision (Unverdi & Tryggvason 1992; Nobari, Jan & Tryggvason 1996; Qian 1997; Pan 2004; Pan & Law 2004). The computation domain was modified from having a symmetric centreplane and full slip wall to one that accommodates a film that has no slip at the wall and can expand outward. The boundary conditions were defined through an extrapolation scheme with first-order accuracy. It is to be noted that in spite of the reduced precision at the extrapolation boundary, the film surface there was not distorted during collision because the domain was large enough that there was no interaction of the outwardly propagating waves with the boundary. Furthermore, in order to adequately resolve the region of impact, the grids in the impact direction were distributed non-uniformly, with a larger number around the colliding interfaces. The minimum grid size was maintained around 0.005.

Figure 1 shows the physical problem and the axisymmetric computation domain. The droplets were initially placed along the z-axis at a distance z_0 prescribed by the experiment. The Navier–Stokes equations were solved for both the gas and liquid phases in a unified domain:

$$\frac{\partial(\rho \boldsymbol{V})}{\partial t} + \nabla\cdot(\rho \boldsymbol{V}\boldsymbol{V}) = -\nabla p + \rho \boldsymbol{g} + \nabla\cdot\frac{1}{Re}(\nabla \boldsymbol{V} + \nabla \boldsymbol{V}^{\mathrm{T}}) - \frac{2}{We}\int_{\Delta s} \kappa \boldsymbol{n}\delta(\boldsymbol{r} - \boldsymbol{r}_f)\mathrm{d}a, \quad (1)$$

where $\boldsymbol{V}$, ρ, and p and t are the velocity, density, pressure and time respectively normalized by V_0, ρ_ℓ, the dynamic pressure $\rho_\ell V_0^2/2$, and R/V_0. In (1) surface tension is added as a delta function, which is the product of three one-dimensional delta functions. It is integrated locally over the immiscible interface within unit volume in order to render a singular force exerted by the liquid surface that is calculated over the entire surface of the droplet and the film. Furthermore, $\rho \boldsymbol{g}$ is the gravitational force that is turned off at a prescribed droplet–film separation before collision, and is merely used to provide the droplet with an initial velocity with the solved velocity field of the surrounding gas, κ is twice the mean curvature, $\boldsymbol{n}$ the outwardly directed unit normal vector at the liquid surface, $\boldsymbol{r}$ the space vector, and the subscript f designates the gas–liquid interface.

The conservation equations of momentum and mass were calculated on a fixed, staggered grid with a second-order central difference scheme for spatial variables and explicit second-order time integration. Since the time step was small in terms of the stability requirement, we usually just carried out first-order time integration (Nobari *et al.* 1996), which was found to simulate the collision event well compared to those obtained by using higher-order schemes. The interface was represented by separate computational points that were moved by the velocity interpolated from the neighbouring grids. These markers were connected to form a front that was used to keep the density and viscosity stratifications sharp and to calculate the surface tension, which was smoothed over the droplet surface in the numerical scheme by using the immersed-boundary method of Peskin (1977) and Unverdi & Tryggvason (1992).

4. Experimental observations

In this section we present the imaged sequences of the impacting droplet. A regime diagram is constructed, with emphasis on the transition from bouncing to absorption, which is similar to the hard collision events between regimes II and III in droplet–droplet collision (Jiang *et al.* 1992). The Weber number corresponding to the transition condition in soft collision, between regimes I and II, is much smaller than that of droplet–droplet collision and could not be identified with sufficient accuracy in the tests.

In the present study we show the influences of the impact inertia and droplet deformation through *We*, and the film thickness relative to the droplet size through the parameter $H_f = h_f/R$. Another physical property of importance, which was not systematically investigated here, is the liquid viscosity because it affects the extent of energy dissipation due to the liquid motion. Its influence can be studied through variations in, say, the Ohnesorge number effected by using liquids of different viscosities. For the liquid used in the present study, and for a typical droplet radius of $R = 300\,\mu\text{m}$, we have $Oh = 0.0277$, while a typical Reynolds number for a velocity of $V_0 = 0.75\,\text{m}\,\text{s}^{-1}$ is $Re = (We/2)^{1/2}/Oh = 78.73$.

4.1. *Characteristic collision dynamics*

Figures 2(*a*) to 2(*c*) respectively show the sequences of bouncing, partial absorption, and (total) absorption for the head-on collision of the droplet with a film of thickness that is about one-tenth the droplet radius, i.e. $H_f \approx 0.1$. The fact that the droplet remains unattached to the film in the bouncing case of figure 2(*a*) is demonstrated by the cuspy, convex curvature (relative to the droplet) of the droplet contour at its base next to the film. This is to be contrasted with the smooth, concave curvature when

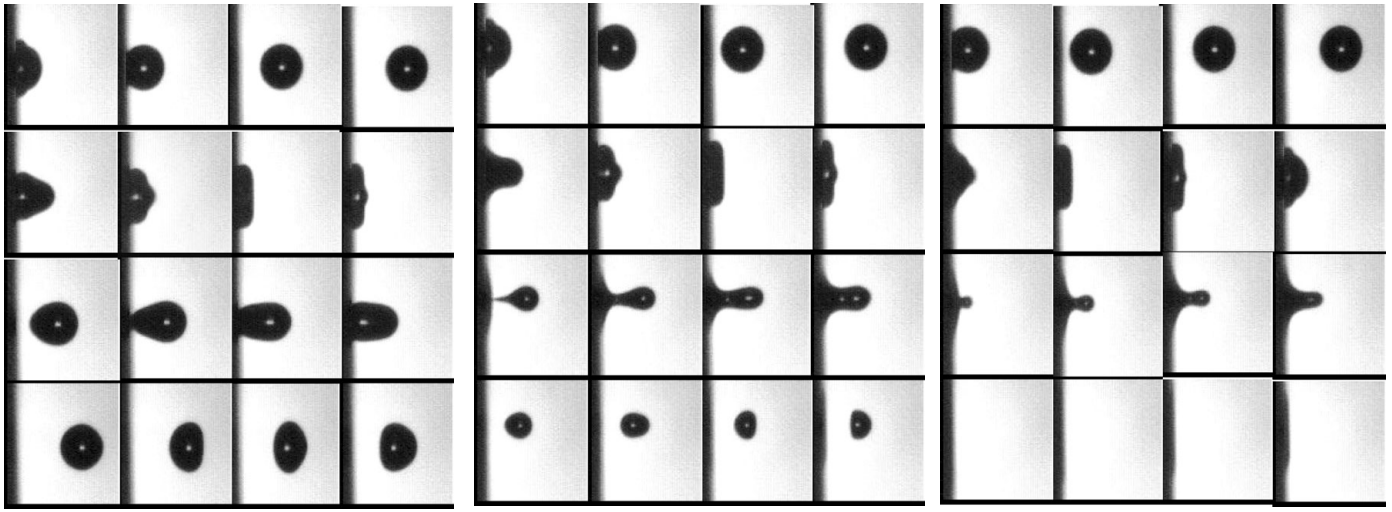

(*a*) (*b*) (*c*)

FIGURE 2. Collision sequences with a shallow layer: (*a*) Bouncing ($R = 278\,\mu\text{m}$, $V = 0.702\,\text{m s}^{-1}$, $H_f = 0.1$, $We = 7.74$); (*b*) partial absorption ($R = 283.5\,\mu\text{m}$, $V = 0.733\,\text{m s}^{-1}$, $H_f = 0.099$, $We = 8.61$); (*c*) absorption ($R = 289\,\mu\text{m}$, $V = 0.756\,\text{m s}^{-1}$, $H_f = 0.096$, $We = 9.32$). Time increment: 0.25 ms.

absorption does occur, as shown in figure 2(*b*) and 2(*c*). Furthermore, occurrence of partial absorption is evident from the reduced size of the ejected droplet compared to that of the incident droplet.

These collision outcomes are analogous to those of regimes II, III, and IV in droplet–droplet collision (Jiang *et al.* 1992), except the occurrence of regimes III and IV is reversed here in that, with increasing *We*, we have bouncing, partial absorption, and total absorption, instead of bouncing, permanent coalescence, and coalescence followed by separation in the droplet–droplet case.

As the film thickness is increased to about the droplet radius such that $H_f \approx 1$, the droplet partially penetrates into the film, with or without merging of the interfaces, as shown in figure 3. Consequently part of the collision image is obstructed by the film and cannot be observed. The global collision outcome, however, can still be discerned. Specifically, if *We* is sufficiently small, the droplet bounces away (figure 3*a*) with the same size as that of the incident droplet, while for larger *We* it is fully absorbed subsequent to the temporary emergence of a tail jet (figure 3*c*). Partial absorption occurs when the film thickness is decreased (figure 3*b*), whereby a secondary droplet of smaller size is ejected above the film surface. These collision events also span longer periods of time than those of the shallow cases shown in figure 2.

4.2. *Regime diagram*

The various collision outcomes described above can be represented in a regime diagram characterized by the collision Weber number *We* and the normalized film thickness H_f, as shown in figure 4 for droplets of different sizes. It is seen that droplets of different sizes investigated herein exhibit the same characteristics of collision outcome. In general, bouncing and absorption respectively occur for small and large values of *We*. This is reasonable based on our understanding of the transition between regimes II and III in droplet–droplet collision. That is, for the smaller *We*, the impact inertia is not sufficient to squeeze out the thin gaseous layer between the colliding interfaces so that they can make contact, while this becomes possible at larger *We*.

However, compared to droplet–droplet collision, the additional system parameter H_f for the film thickness and the presence of the solid surface supporting the thin film introduce an additional collision response that is rather interesting. That is, in an intermediate range of *We*, the outcome is non-monotonic with increasing H_f. To be more specific, first consider the small droplet case of figure 4(*a*), with $R = 165\,\mu\text{m}$. It is seen that, for a thin film of sufficiently small H_f, say $H_f \lesssim 0.8$, the transition *We* between bouncing and absorption increases with increasing H_f, approaching an approximately constant value of about 14. On the other hand, for the thick-film situations of sufficiently large H_f, say $H_f \gtrsim 1.2$, the transition *We* not only becomes independent of H_f, but it also attains the same constant value of about 14. It is of particular interest to note that this value is about the same as that for the transition between regimes II and III in droplet–droplet collision (Jiang *et al.* 1992; Qian & Law 1997). Furthermore, partial absorption was not observed for this droplet size.

In the intermediate range of $0.8 \lesssim H_f \lesssim 1.2$, for which the film thickness is comparable to the droplet radius, the response becomes non-monotonic with respect to H_f. Specifically, within the range of $10 < We < 14$, increasing H_f from a small value leads to a triple reversal: absorption, to bouncing, to absorption again, and to bouncing again. This triple reversal is manifested by the presence of an 'absorption peninsula' that punctuates the otherwise constant transition boundary of $We_c \approx 14$, beyond which absorption is favoured. Furthermore, the lower boundary of this

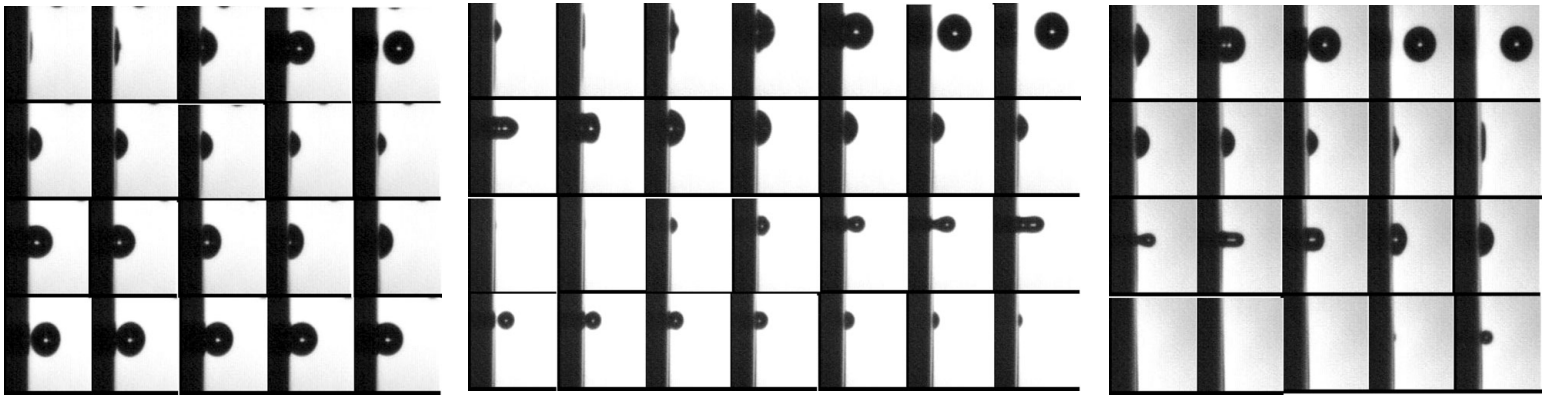

FIGURE 3. Collision sequences with a deep layer (film thickness close to the droplet radius): (*a*) Bouncing ($R = 270\,\mu$m, $V = 0.764\,\mathrm{m\,s^{-1}}$, $H_f = 0.84$, $We = 8.89$); (*b*) partial absorption ($R = 295.5\,\mu$m, $V = 0.764\,\mathrm{m\,s^{-1}}$, $H_f = 0.768$, $We = 9.75$); (*c*) absorption ($R = 295.5\,\mu$m, $V = 0.773\,\mathrm{m\,s^{-1}}$, $H_f = 0.98$, $We = 9.97$). Time increment: 0.25 ms.

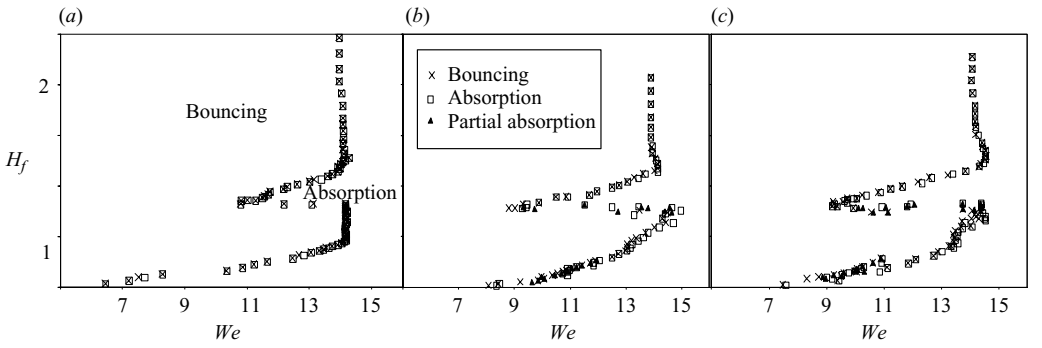

FIGURE 4. Distribution of the typical regimes on an H_f–We plot for droplets of different sizes: (*a*) $R \approx 165\,\mu\text{m}$; (*b*) $R \approx 250\,\mu\text{m}$; (*c*) $R \approx 305\,\mu\text{m}$.

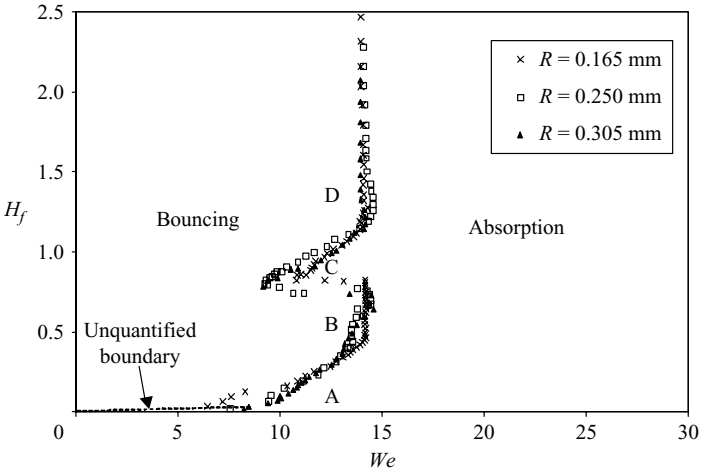

FIGURE 5. A regime diagram with universal characteristics on an H_f–We plot.

peninsula is fairly flat with respect to We, while the upper boundary increases with increasing We.

For the larger droplet sizes of $R = 250$ and $305\,\mu\text{m}$, figures 4(*b*) and 4(*c*) show that the general characteristics of the regime boundaries separating bouncing and absorption are the same. Partial absorption, however, is now observed, occurring over the entire lower boundary of the absorption peninsula as well as the lower segment of the transition boundary for the thin-film regime of $H_f \lesssim 0.8$. Furthermore, it occurs over a very narrow range in H_f with values only slightly smaller than those for the transition to total absorption. Because of the narrowness of this regime, and the inevitable scatter in the experimental data, the transition boundaries for partial absorption and total absorption cannot be clearly resolved.

We note in passing that our observation that partial absorption occurring only for large droplets is in agreement with the results of Rein (1993), who used large droplets ($R > 1\,\text{mm}$) and concluded that the transition to total absorption usually begins with partial absorption.

We next plot in figure 5 all the data of figure 4 for different droplet sizes. It is seen that they roughly collapse into a narrow band, with the only exception being a narrower peninsula for the small droplet. The closeness of this correlation indicates

the fundamental significance of H_f and *We* as the controlling parameters for the droplet–film collision phenomena.

The presence of the absorption peninsula and the phenomenon of triple reversal are perhaps the most interesting experimental observations of the present investigation. We shall show in due course, through figures 10, 11, 13, and 14 as well as additional discussions, that the droplet dynamics at the state of interface merging are fundamentally different for the transition across the various boundaries.

There are several possible regimes not observed or covered in the present investigation. First, as $We \rightarrow 0$, it is reasonable to expect that the droplet will be absorbed by the film. Second, because of the limitation on the maximum *We* attainable with the present experimental setup, we did not observe the phenomena of splashing and fragmentation (Rein 1993; Stanton & Rutland 1998) associated with very large-*We* collisions. Finally, since the film thickness could not be determined accurately for values smaller than about 10 μm, the ultra-thin regime is marked by an unquantified boundary in figure 5.

5. Characteristics of the bouncing–merging transition

In addition to the collision images and regime diagrams presented above, further understanding of the underlying physics governing collision can be gained through computational simulation of the collision event. In particular, it is only through computation that the dynamics of the very narrow interfacial region between the droplet and the film, and the motion within the droplet and the film, can be resolved. It will be demonstrated that the global collision dynamics is intimately affected by these motions at the small scale. The simulation, based on continuum mechanics, is however inherently unable to describe the final stage of rupturing and consequently merging of the interfaces, which would require descriptions based on rarefied gas dynamics and molecular attractive force, as discussed in Pan (2004) and Pan & Law (2004) for the droplet–droplet studies.

5.1. *Comparison of global collision images*

We first compare the simulated and experimental collision sequences in order to demonstrate the validity of the simulation. Since the simulation does not include surface rupturing and hence merging, we first compare bouncing collisions. To facilitate the discussion, we shall use both the real time and a scaled time t, which is the real time divided by the characteristic droplet oscillation time (Lamb 1932), $T = 2\pi(\rho_\ell R^3/8\sigma)^{1/2}$. We also note that since the simulated images shown are the frontal views of the cross-sectional contours at the centreplane, contours of those segments that indent inward could not be photographically imaged because they were obstructed by the corresponding segments at the rim.

Figures 6 and 7 respectively show comparisons for typical soft and hard collisions, for small and large *We*, respectively. It is seen that the experimental images are simulated well in terms of the droplet shape and phase, particularly the motion of the rearward face of the droplet. Furthermore, the simulation also reveals features of the global collision that cannot be experimentally observed. Specifically, while the rearward surface for the soft collision mostly maintains a bulging contour during the impact, during hard collision a prominent dimple is induced over this surface upon impact, as shown in the fifth image of figure 7. This dimple, whose view is obstructed by the rim surrounding it in the experimental image, is caused by the strong forward motion of the droplet and the physical barrier of the film in restraining the motion of the frontal surface.

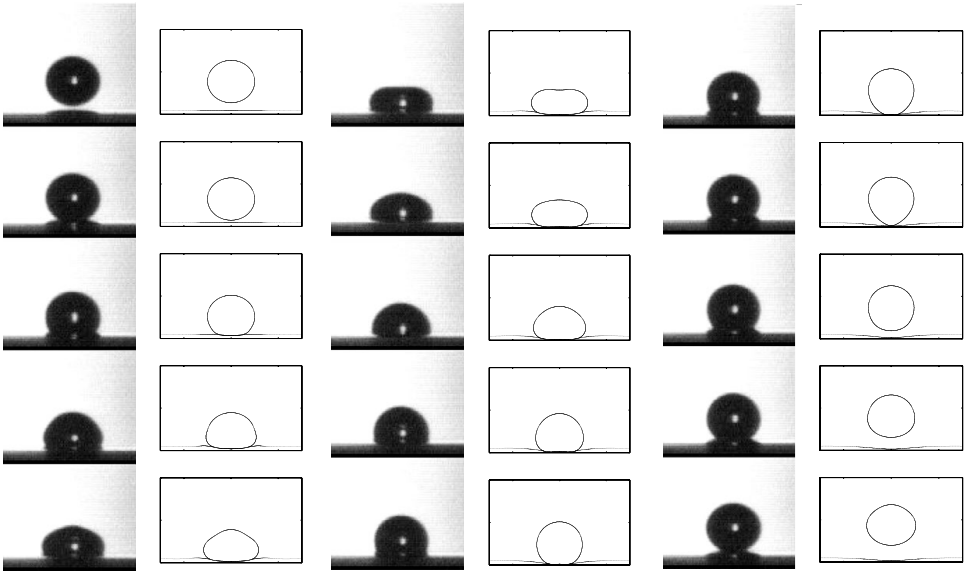

FIGURE 6. Collision sequences determined by the experiment (left) and simulation (right) for $H_f = 0.18$ and $We = 1.79$, time increment $= 0.25$ ms ($\Delta t = 0.12$).

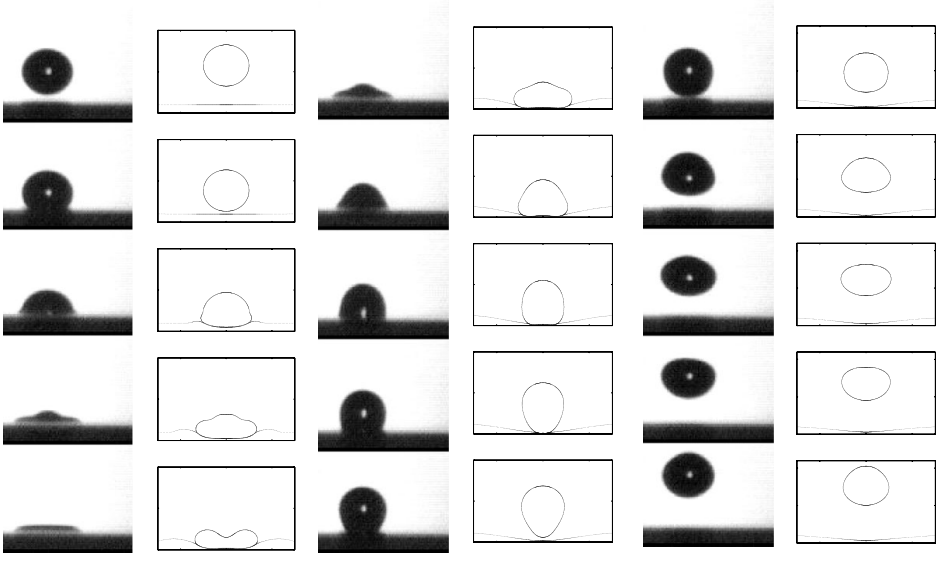

FIGURE 7. Collision sequences determined by the experiment (left) and simulation (right) for $H_f = 0.392$ and $We = 8.49$, time increment $= 0.25\,\mathrm{m\,s^{-1}}$ ($\Delta t = 0.13$).

We further note from figure 8(a) that as the droplet approaches the film, its forward surface is gradually flattened and eventually becomes indented at the centre. Such an indentation, or 'dimple', has been frequently observed during the drainage of axisymmetric films (Middleman 1995; Yiantsios & Davis 1990). This is a consequence of the pressure build-up in the interfacial region, relative to the pressure in the droplet interior, because owing to viscosity the gas between the interfaces cannot be readily

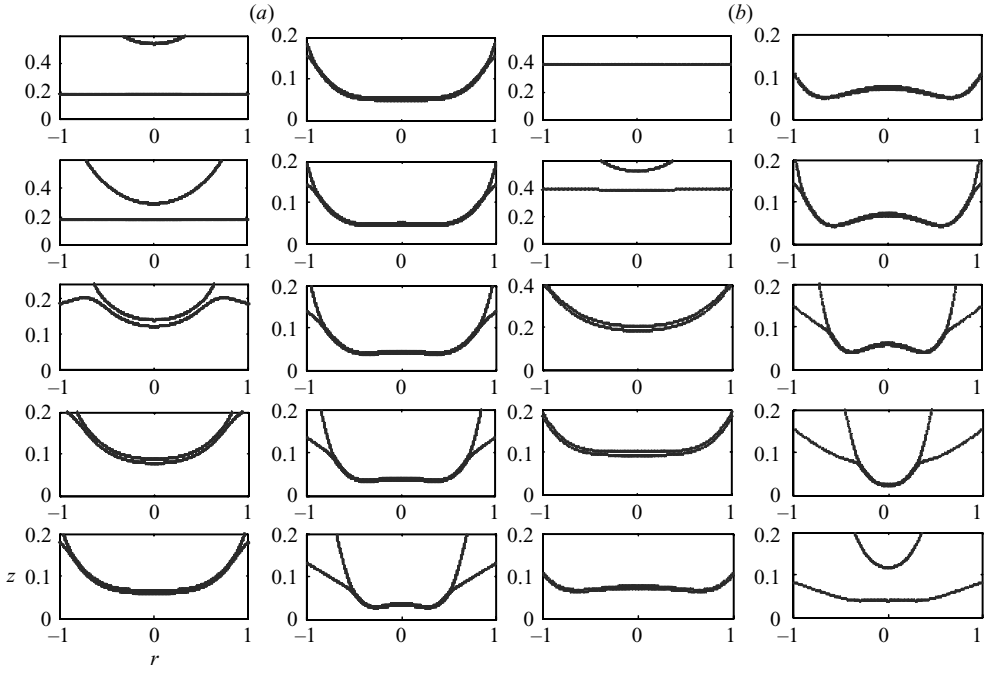

FIGURE 8. Magnified views of the colliding interface region for the images in (*a*) figure 6 and (*b*) figure 7.

drained away. A similar mechanism also applies to the flow within the liquid film in that, if the film thickness is small, the fluid cannot be readily drained out and subsequently the pressure is increased. Furthermore, this increase is larger than that in the gas gap such that the centre portion of the film bulges, as shown in the right-hand column of figure 8(*a*). When *We* is larger (figure 8*b*), the stronger impact leads to more substantial deformation of the droplet and film surfaces, with a more prominent indentation on the bottom surface of the droplet. When this indentation is eventually relieved as the droplet starts to recede, the forward thrusting motion of the relieved mass pushes the central surface toward the bottom as it bounces off.

We next study the collision events in which the interfaces merge. Figure 9(*a*) shows the experimental sequence for the collision with a thin film so that the merging event can be photographed without obstruction. The corresponding computed results without merging of the interfaces are shown in figure 9(*b*). Since the fluids inside the droplet and film are not exchanged during collision for the simulated bouncing case, the droplet mass is conserved.

Since merging did occur experimentally, it is of interest to identify the instant and state of the droplet when it occurs, using the experimental images as a guide. To this end we first plot in figure 10 the temporal variation of the locations of the droplet surface at the centre and the rim, each normalized by R, as H_{centre}, and, H_{rim}. It is seen that around $t \approx 0.25$ the closest approach of the droplet surface to the solid wall switches from the centre to the rim, indicating that the forward surface of the droplet, in the interfacial region, becomes indented at its centre due to the pressure buildup. The extent of indentation becomes progressively more severe until $t \approx 0.5$ when the surface at the centre starts to recede and hence relieves this pressure buildup. As will be shown later this state can be considered to be that of maximum deformation in

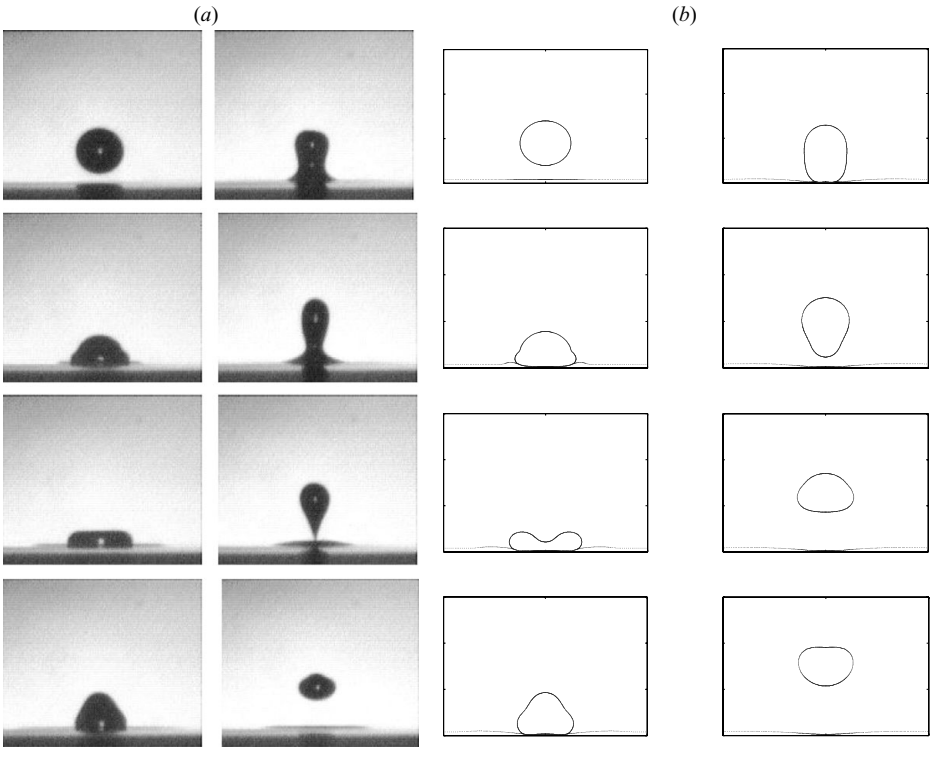

FIGURE 9. The sequence of partial absorption with $R = 305\,\mu\text{m}$, $V = 0.691\,\text{m}\,\text{s}^{-1}$, $H_f = 0.165$, $We = 8.22$, $T = 1.984$, and time difference $0.5\,\text{m}\,\text{s}^{-1}$ ($\Delta t = 0.252$) obtained by (a) experiment and (b) numerical simulation without merging.

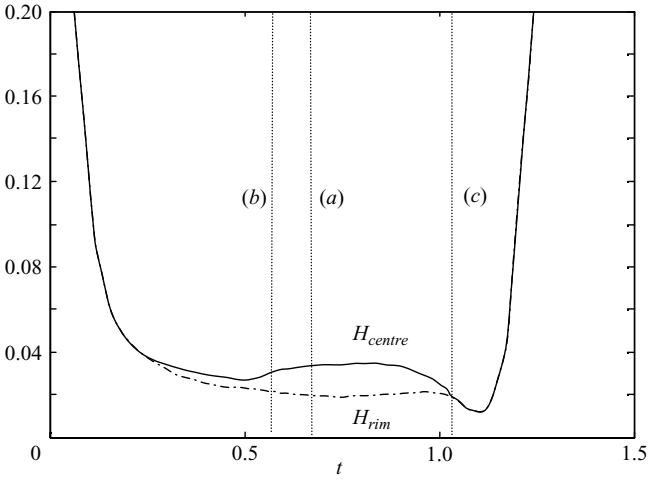

FIGURE 10. The evolutions for $H_f = 0.165$, $We = 8.22$ of the centre (solid line) and the lowest location of the bottom droplet surface (dashed line), with the rupture instants of figure 11(a) to 11(c) indicated by the vertical line.

terms of the droplet surface energy. The droplet subsequently contracts and the radius of the rim continuously shrinks until the indentation is relieved at $t \approx 1.05$, causing the lowest point of approach to switch back to the centre of the forward surface.

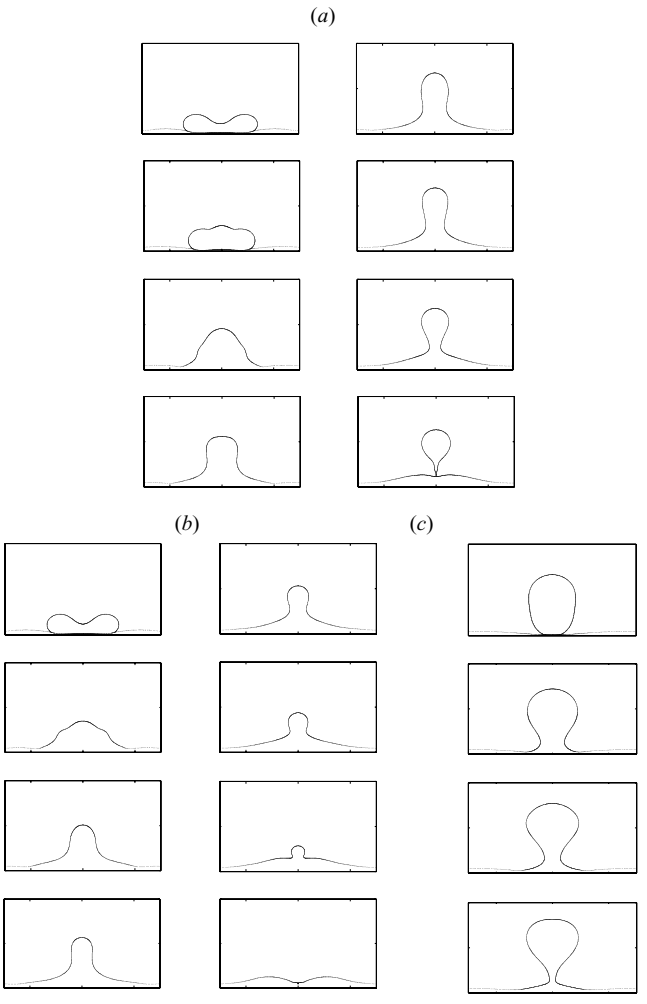

FIGURE 11. The computational sequences of partial absorption ($H_f = 0.165$, $We = 8.22$, $\Delta t = 0.125$) with different rupture times, t_{rup}: (*a*) 0.653, (*b*) 0.571, and (*c*) 1.051.

To study the characteristics and effects of merging, and since the present continuum mechanics formulation is intrinsically unable to describe molecular phenomena through which the surface molecules are attracted to each other leading to the destruction of distinct surface boundaries, we follow the approach of Nobari *et al.* (1996) by simply manually connecting the surfaces. In order to identify the instant when merging is effected, we have chosen three possible instants, designated by (*a*), (*b*), and (*c*), in figure 10, to rupture the interfaces and simulate the ensuing motion that leads to the breakup of the neck connecting them. The results are then compared with the sequence of the experimental images showing partial absorption, recognizing that the imposition of an incorrect merging instant will lead to correspondingly incorrect surface contours of the droplet compared to those of the experimental images.

Figure 11(*a*) shows the sequence of neck shrinkage with the rupture time t_{rup} being 0.653 which, lying between the third and fourth frames in figure 9(*a*) and 9(*b*), is between the maximum deformation and the relief states as identified in figure 10. It is seen that the computation simulates moderately well the experimental images subsequent to the instant of the artificial rupture. On the other hand, by imposing

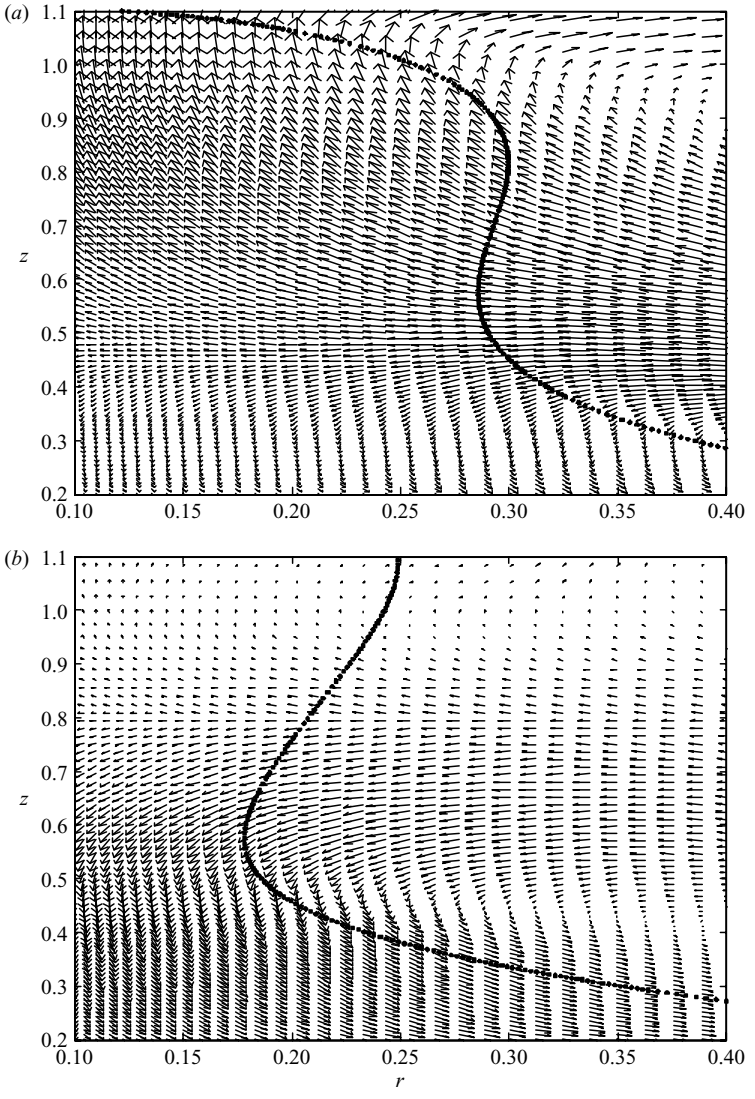

FIGURE 12. The interface shape and velocity vectors after merging is implemented at $t = 0.653$ ($H_f = 0.165$, $We = 8.22$): (a) $t = 0.903$ and (b) $t = 1.153$.

an earlier rupture time, $t_{rup} = 0.571$ (figure 11b), it is seen that most of the droplet fluid is drawn into the film after merging and the resulting bouncing inertia is much weaker. Consequently a shrinking neck cannot be formed and the collision ends in total absorption, accompanied by the creation of an outwardly propagating surface wave over the film. The evolution is similar to that of figure 2(c). Finally, if the rupture is delayed to the stage when the indentation is relieved, with $t_{rup} = 1.051$ (figure 11c), more mass and energy are retained for bouncing and a larger bulb is formed, resulting in the eventual emission of a larger secondary droplet. The above result therefore demonstrates that, for $H_f \ll 1$, surface rupturing and hence merging occur when the droplet is indented.

The phenomenon of pinching shown in figure 11(a) is further characterized by noting that a fraction of the rebounded fluid still moves upward after merging while the rest is pulled back into the film, as shown by the velocity vectors in figure 12(a).

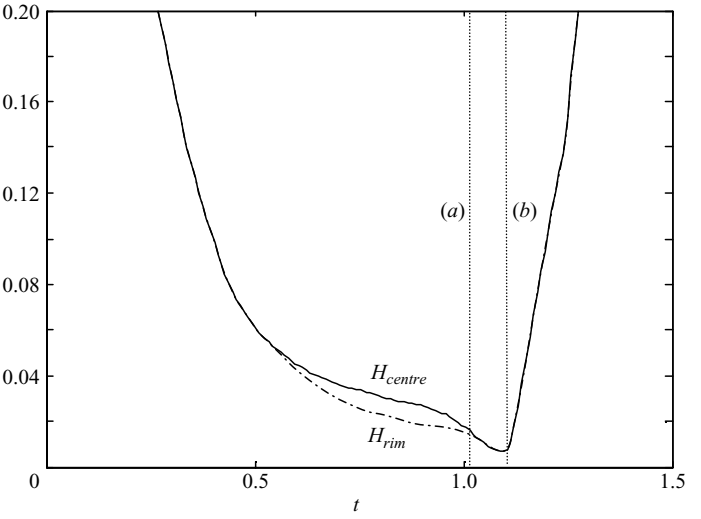

FIGURE 13. The evolutions for $H_f = 0.768$, $We = 9.75$ of the centre (solid line) and the lowest location of the bottom droplet surface (dashed line), with the rupture instants of figures 14(*a*) and 14(*b*) indicated by the vertical lines.

Since the bouncing inertia of the upward flow is large enough to overcome the pull of the surface tension, the fluids moving in opposite directions continue their respective downward and upward motions. Consequently the pressure at the neck decreases and the interface shrinks. As shown in figure 12(*b*), the neck becomes thinner and at a certain time is pinched off.

For collision with a larger H_f, most of the forward part of the droplet is submerged in the film, rendering it impossible to image and hence identify the instant of surface rupture as indicated by the change in the interfacial surface curvature. Consequently the droplet contour for the submerged portion and period can only be calculated. On the other hand, in the event of partial absorption, the motion and contour of the emitted secondary droplet, which depend on the droplet dynamics and history during the submerged phase, can still be compared when it emerges from the film. This is demonstrated in the following.

Figures 13 and 14 respectively show the interface locations for figure 3(*b*) and the simulated images with different rupture times. It is seen that rupturing of the surfaces, with the formation of a secondary droplet, must occur subsequent to the relief of the indentation (figures 13 and 14*b*) because otherwise the collision ends in complete absorption (figure 14*a*). These results thus demonstrate that merging for the thick-film cases is a consequence of the thrusting of the relieved surface fragment of the droplet, moving it closer to the film surface.

5.2. *Collision dynamics in different regimes*

Perhaps the most interesting and initially unexpected result from the present experiment is the existence of the absorption peninsula and consequently the triple reversal in terms of bouncing and absorption with increasing film thickness. The absorption peninsula therefore partitions the collision response into four distinct regimes, indicated by A (absorption), B (bouncing), C (absorption), and D (bouncing) in figure 5. We have systematically investigated the characteristics of these four

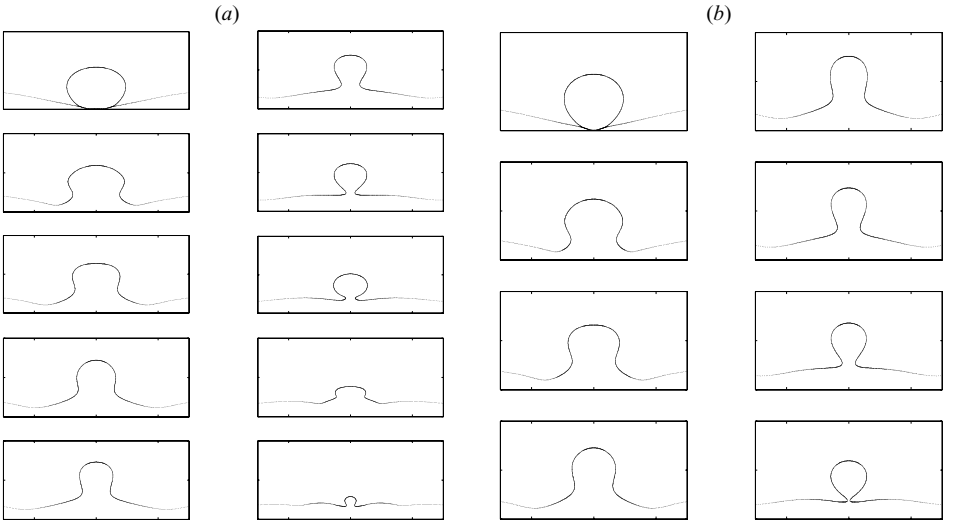

FIGURE 14. The computational sequences of partial absorption in figure 3(*b*) ($H_f = 0.768$, $We = 9.75$, $T = 1.897\,\mathrm{m\,s^{-1}}$) with different rupture times, t_{rup}: (*a*) 1.006 and (*b*) 1.100. Time increment: $0.25\,\mathrm{m\,s^{-1}}$ ($\Delta t = 0.132$).

regimes by performing calculations for a fixed $We = 12.27$, with increasing H_f of about 0.2, 0.5, 1.0, and 1.5. Results for these four regimes are sequentially presented in figures 15 to 18, showing the locations of the closest approach of the droplet surface to the restraining, bottom surface, and the energy budget.

In order to interpret the triple reversal response, we first recognize the dominant role of the solid surface in providing a fixed physical barrier to the fluid and hence droplet motion. Since it is unyielding, its presence accentuates the impact inertia of the droplet, hence promoting drainage of the gas in the interfacial region and consequently merging.

Another major factor affecting the collision outcome is the energy transfer from the droplet to the film through the displacement of the film. This transfer reduces the droplet inertia and consequently its ability to approach closely the film surface to effect merging. The amount of energy transfer is expected to increase with the film thickness, but would become saturated when it is of the order of the droplet size.

To quantify the energy transfer between the droplet and the film that may affect the bouncing–merging transition, we have computed the evolution of the energy budget, noting that the total energy of the flow field consists of surface energy, kinetic energy, and the cumulative viscous dissipation energy. Viscous loss is computed through evaluation of the viscous dissipation rate, given by (White 1991)

$$\Phi = \mu\left[2\left(\frac{\partial u}{\partial r}\right)^2 + 2\left(\frac{u}{r}\right)^2 + 2\left(\frac{\partial w}{\partial z}\right)^2\right] + \mu\left(\frac{\partial u}{\partial z} + \frac{\partial w}{\partial r}\right)^2 - \frac{2}{3}\mu\left[\frac{1}{r}\frac{\partial (ru)}{\partial r} + \frac{\partial w}{\partial z}\right]^2, \tag{2}$$

which consists of three sources, respectively representing effects due to normal strain, shear strain, and volumetric dilatation.

With the above, we now interpret the triple reversal response shown in figure 5. Starting from regime A, the restraining effect of the solid surface is expected to be most severe here because the film is very thin ($H_f = 0.198$). It is seen that reduction

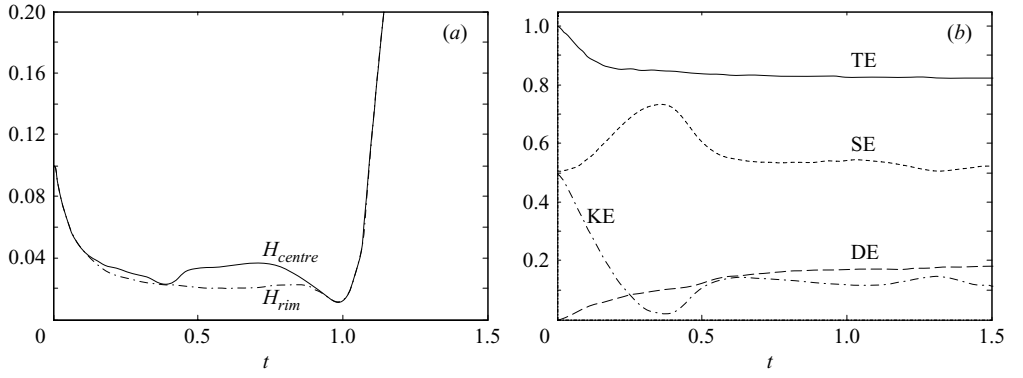

FIGURE 15. $R = 318\,\mu\text{m}$, $V = 0.827\,\text{m s}^{-1}$, $H_f = 0.198$, $We = 12.27$, $T = 2.117\,\text{m s}^{-1}$. (*a*) Centre (solid line) and lowest locations (dashed line) of the bottom surface of the droplet, and (*b*) energy components of the droplet: TE is the total energy, SE the surface energy, KE the kinetic energy, and DE the cumulative viscous dissipation energy.

of the total energy of the droplet (figure 15*b*) occurs most significantly in the initial period, for $0 \lesssim t \lesssim 0.2$. During this period intrusion of the droplet into the film, as indicated by the substantial reduction in the location of the frontal surface (figure 15*a*) and deformation of the shape of the droplet from spherical, are most prominent. This amount of kinetic energy is transferred to the deformation and motion of the film. After this period of film intrusion, the total energy of the droplet remains fairly constant. Substantial deformation of the droplet, however, continues, as indicated by the steady increase in the surface energy and the corresponding decrease in the kinetic energy, until the state ($t \approx 0.375$) at which the surface energy is the largest while the kinetic energy smallest, occurring when the upper surface of the droplet is most indented. Subsequent to this state of maximum deformation, at which the surface energy is at its maximum, the droplet starts to contract due to surface tension such that, from $t \approx 0.375$ to $t \approx 0.625$, the surface energy decreases, the kinetic energy increases, and the droplet as a whole starts to bounce off. Furthermore, during the entire period of $0 \lesssim t \lesssim 0.625$, there is substantial motion inside the droplet, leading to a steady increase in the total viscous loss.

After $t \approx 0.625$, transfer of energy among different modes is relatively small, and is primarily due to oscillation of the global shape of the droplet as it strives to restore sphericity through internal viscous dissipation.

In reality, collision in this regime results in interface merging and total absorption. The mechanism responsible for merging in the present regime is similar to that for regime III in droplet–droplet collision, namely draining of the interfacial gas gap is facilitated by the strong restraining influence of the bottom wall for the present case and the symmetry plane for the droplet–droplet case. Consequently the interface at the rim of the indentation can approach the surface of the film so closely that the molecular attraction force becomes effective. Because of the rigidity of the bottom surface for the present situation compared to the deformable counterpart in droplet–droplet collision, which tends to trap more gas and enhance bouncing, the critical *We* is lower for droplet–film collision and approaches zero as H_f is decreased.

For the response in regime B (figure 16), the film is thicker ($H_f = 0.495$), the influence of the rigid bottom is smaller, and consequently the extent of deformation is reduced. Specifically, calculations showed a smaller dimple over the rearward surface

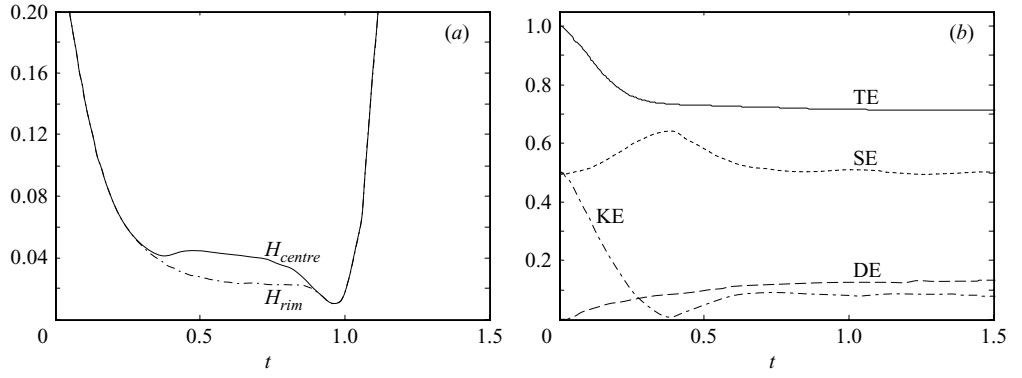

FIGURE 16. As figure 15 but for $H_f = 0.495$.

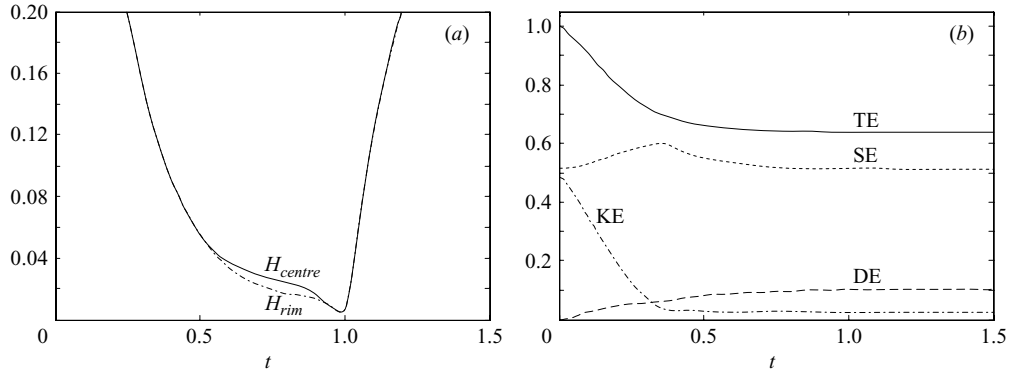

FIGURE 17. As figure 15 but for $H_f = 0.991$.

and reduced elongation during the rebounding phase. Furthermore, for the thicker film there is a greater amount of energy transfer from the droplet, as shown by the smaller value of the total energy after energy transfer is mostly completed (figure 16*b*). In this case the droplet does not have sufficient momentum to squeeze out the gas in the inter-droplet gap to cause surface rupture, and subsequently bounces away. The transition from regime A to regime B is therefore similar to that from regime III to regime II in droplet–droplet collision, being caused by a reduction in the effective impact inertia.

The trend of reduced deformation and increased energy loss from regimes A to B continues to regime C ($H_f = 0.991$, figure 17), for which the film thickness is comparable to the droplet radius. In this regime, however, the influence of the bottom restraining surface is felt only when the droplet has largely penetrated the film. Consequently the pressure build-up in the interfacial region is reduced, as demonstrated by the shorter period over which the interfacial indentation is present as well as the milder indentation, as shown by the smaller difference between H_{centre} and H_{rim} in figure 17(*a*). A greater penetration can therefore be achieved.

Recognizing that the film can be considered to be respectively relatively thin and thick for regimes A and C, detailed studies in the manner of the previous section on the merging in thin and thick films have subsequently shown that surface rupture occurs at the droplet rim in regime A, as the droplet is still globally moving forward.

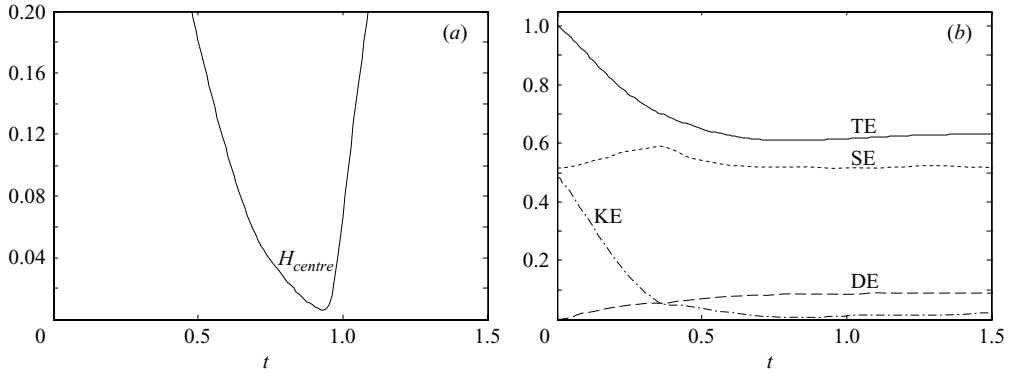

FIGURE 18. As figure 15 but for $H_f = 1.486$.

However, rupturing and merging in regime C occur at the centre as a consequence of the relief of the indentation when the droplet starts to recede from the film. The forward thrusting of the relieved mass allows it to reach close to the film surface to effect merging. Indeed, the switch of the merging location from the rim to the centre caused by the thrusting action associated with the appropriate film thickness could be the cause of the somewhat flatness of transition boundary between regimes B and C as H_f increases.

Finally, with $H_f \gtrsim 1$ for regime D ($H_f = 1.486$, figure 18), the influence of the bottom surface is very much reduced. In particular, the surface of the film in the inter-droplet region can be readily displaced. This is substantiated by the absence of indentation (figure 18*a*) over the droplet surface in this regime. Consequently bouncing is observed.

The above results also show that energy transfer to the film appears to reach an almost constant value subsequent to the initial deformation. In figure 19(*a*) we have plotted this 'constant' value, evaluated at $t = 1.5$, as a function of H_f for the case of $We = 12.26$. It is seen that the energy transferred to the film increases with increasing H_f, but reaches a maximum at $H_f \approx 1$. For larger H_f, there is a slight increase in E because a small amount of the energy is returned to the droplet as the displaced film contracts (figure 18*b*). This is shown in figure 19(*b*) as the difference of the droplet energy at $t = 1.5$ and its minimum value as a function of H_f. It is seen that this interaction saturates for $H_f \gtrsim 2.5$, which can thus be considered as the limit of a deep pool. Since this amount of returned energy is very small, we can also consider that the energy transfer to the film is saturated when $H_f \approx 1$, which is physically reasonable. Finally, figure 19(*c*) shows that the maximum droplet deformation decreases with increasing film thickness, reaching a near constant value when $H_f \approx 1$.

5.3. *Relaxation times for droplet and film*

The above results show that the energy transfer from the droplet to the film becomes progressively more effective as the film thickness approaches the droplet radius, $H_f \to 1$. This effect can also be interpreted on the basis of the characteristic oscillation frequencies of the droplet and the film. For the droplet, it is given by $\omega_d = (8\sigma/\rho_\ell R^3)^{1/2}$. For a film of depth h_f and in the absence of gravity, the dispersion relation subject to disturbance is $\omega_f = [(\sigma k^3/\rho_\ell)\tanh(kh_f)]^{1/2}$ (Kundu & Cohen 2002), where k is the wavenumber of the disturbance. For a droplet impacting a surface, the wavelength

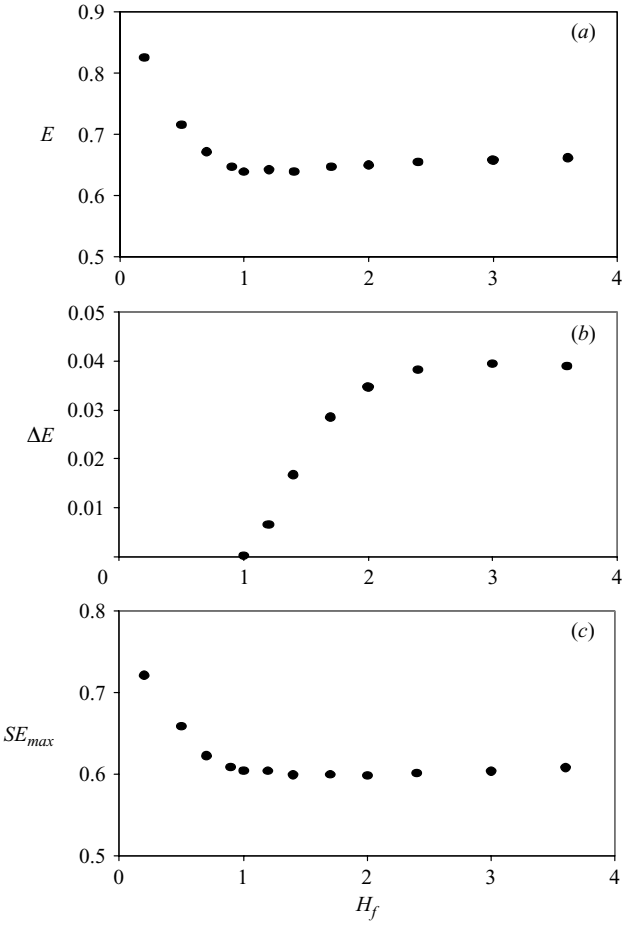

FIGURE 19. The variation of different energy evaluations with respect to H_f ($R = 167\,\mu\text{m}$, $V = 1.140\,\text{m s}^{-1}$, $H_f = 1.486$, $We = 12.26$): (a) Total energy of the droplet at $t = 1.5$; (b) the difference between the energy at $t = 1.5$ and the minimum energy of the droplet; (c) the maximum surface energy of the droplet.

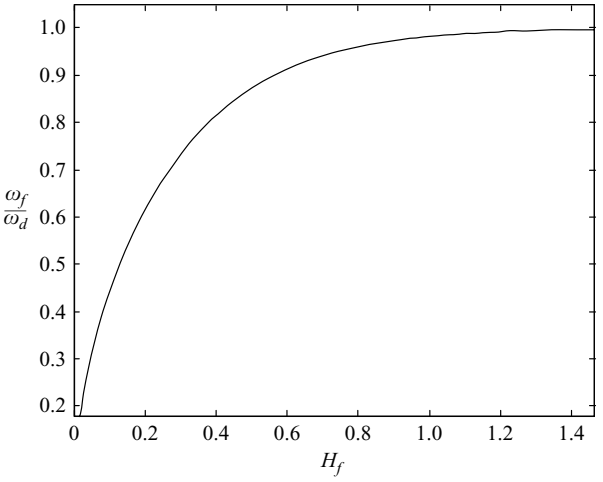

FIGURE 20. The variation of ω_f/ω_d for $\lambda = \pi R$ with respect to H_f.

of the disturbance can be considered to be the circumference of the hemisphere, namely πR, which then yields $k = 2/R$. Consequently we have $\omega_f = \omega_d\ [\tanh(2H_f)]^{1/2}$. Figure 20 plots ω_f/ω_d as a function of H_f. It is seen that $\omega_f \to \omega_d$ as $H_f \to 1$. In particular for the range $0.8 \lesssim H_f \lesssim 1.2$, which approximately corresponds to the peninsula regime (figure 5), ω_f/ω_d is between 0.96 and 0.99.

This correspondence in the characteristic oscillation frequencies for the droplet and the film then implies that not only is the transfer of energy from the droplet to the film most efficient when $H_f \approx 1$, but the penetration into the film is also facilitated. As discussed earlier, these two factors respectively retards and promotes the approach of the droplet surface to the film surface, and hence the propensity to merge.

6. Concluding remarks

In the present investigation the dynamics of the head-on collision of a droplet with a liquid film of the same material, backed by a solid surface, was studied experimentally and computationally, with emphasis on the propensity of bouncing of the droplet versus its absorption by the film. Extensive experimentation was performed for the collision outcome, and a regime diagram was constructed in terms of the impact droplet Weber number, *We*, and the film thickness relative to the droplet radius, H_f, which were shown to correlate well with the collision response. Results show that while bouncing and absorption are respectively favoured for small and large *We*, absorption is further facilitated for $H_f \ll 1$ and $H_f \approx 1$. Consequently there exists a range of *We* over which increasing H_f from $H_f \ll 1$ results in a triple reversal in the collision response, from absorption, to bouncing, to absorption again, and to bouncing again. Partial absorption with the emission of a secondary droplet with a size smaller than that of the original droplet was also observed, being favoured for larger droplets and in a narrow regime in the transition boundary between bouncing and total absorption for $H_f \approx 1$. By computationally simulating these collision events and studying the extent of droplet deformation, the dynamics of the interfaces, and the energy budget, the influence of the rigidity of the backing surface for the film and the efficiency of the transfer of energy from the droplet to the film on droplet bouncing and absorption were identified. It was also found that surface rupture occurs at the rim and centre in the interfacial region for collision with small and large H_f respectively.

The work was supported by the Air Force Office of Scientific Research under the technical monitoring of Dr M. Birkan. We thank Professor S. H. Lam for stimulating discussions and Mr D. L. Zhu for his help with the experimentation.

REFERENCES

Ashgriz, N. & Poo, J. Y. 1990 Coalescence and separation in binary collisions of liquid drops. *J. Fluid Mech.* **221**, 183.

Ching, B., Golay, M. W. & Johnson, T. J. 1984 Droplet Impacts upon liquid surfaces. *Science* **226**, 535.

Harlow, F. H. & Shannon, J. P. 1967 The splash of a liquid drop. *J. Appl. Phys.* **38**, 3855.

Jayaratne, O. W. & Mason, B. J. 1964 The coalescence and bouncing of water drops at an air/water interface. *Proc. R. Soc. Lond.* A **280**, 545.

Jiang, Y. J., Umemura, A. & Law, C. K. 1992 An experimental investigation on the collision behaviour of hydrocarbon droplets. *J. Fluid Mech.* **234**, 171.

Kundu, P. K. & Cohen, I. M. 2002 *Fluid Mechanics*, 2nd Edn. Academic.

Lamb, H. 1932 *Hydrodynamics*. Dover.

Middleman, S. 1995 *Modeling Axisymmetric Flows: Dynamics of Films, Jets, and Drops*. Academic.

Nobari, M. R., Jan, Y.-J. & Tryggvason, G. 1996 Head-on collision of drops – A numerical investigation. *Phys. Fluids* **8**, 29.

Orme, M. 1997 Experiments on droplet collisions, bounce, coalescence and disruption. *Prog. Energy Combust. Sci.* **23**, 65.

Pan, K. L. 2004 Dynamics of droplet collision and flame-front motion. PhD thesis, Princeton University.

Pan, K. L. & Law, C. K. 2004 On the dynamics of head-on droplet collision: experiment and simulation. *AIAA Paper* 2004–1159.

Peskin, C. S. 1977 Numerical analysis of blood flow in the heart. *J. Comput. Phys.* **25**, 220.

Qian, J. 1997 Droplet and flame dynamics in combustion phenomena. PhD thesis, Princeton University.

Qian, J. & Law, C. K. 1997 Regimes of coalescence and separation in droplet collision. *J. Fluid Mech.* **331**, 59.

Rein, M. 1993 Phenomena of liquid drop impact on solid and liquid surfaces. *Fluid Dyn. Res.* **12**, 61.

Rodriguez, F. & Mesler, R. 1985 Some drops don't splash. *J. Colloid Interface Sci.* **106**, 347.

Stanton, D. W. & Rutland, C. J. 1998 Multi-dimensional modeling of thin liquid films and spray-wall interactions resulting from impinging sprays. *Intl J. Heat Mass Transfer* **41**, 3037.

Stow, C. D. & Hadfield, M. G. 1981 An experimental investigation of fluid flow resulting from the impact of a water drop with an unyielding dry surface. *Proc. R. Soc. Lond.* A **373**, 419.

Unverdi, S. O. & Tryggvason, G. 1992 A front tracking method for viscous, incompressible, multi-fluid flows. *J. Comput. Phys.* **100**, 25.

White, F. M. 1991 *Viscous Fluid Flow*, 2nd Edn. McGraw-Hill.

Yiantsios, S. G. & Davis, R. H. 1990 On the buoyancy-driven motion of a drop towards a rigid surface or a deformable interface. *J. Fluid Mech.* **217**, 547.